Optical Materials 159 (2025) 116581

Contents lists available at ScienceDirect

Optical Materials

journal homepage: www.elsevier.com/locate/optmat

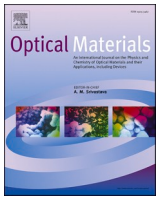

Research Article

Influence of Er^{3+} concentration and sintering temperature on structural and spectroscopic properties of $BaTiO_3$:Er^{3+}

Zorica Ž. Lazarević [a,*], Aleksandra Milutinović [a], Milica Ćurčić [a], Maja S. Rabasović [a], Ivana Stajčić [b], Boško Ćosić [a,c], Uroš Ralević [a], Novica Paunović [a], Branka Hadžić [a], Bojana Simović [d], Dalibor Sekulić [e], Vesna Paunović [f]

[a] Institute of Physics, University of Belgrade, Pregrevica 118, Zemun, Belgrade, Serbia
[b] University of Belgrade, Department of Physical Chemistry, Vinca Institute of Nuclear Sciences, Mike Petrovica Alasa 12-14, 11351, Vinca, Belgrade, Serbia
[c] Senzor Infiz DOO Beograd-Zemun, Pregrevica 118, Zemun, Belgrade, Serbia
[d] University of Belgrade, Institute for Multidisciplinary Research, Kneza Viseslava 1, 11030, Belgrade, Serbia
[e] Faculty of Technical Sciences, University of Novi Sad, Novi Sad, Serbia
[f] University of Niš, Faculty of Electronic Engineering, Aleksandra Medvedeva 4, Niš, Serbia

ARTICLE INFO

Keywords:
$BaTiO_3$
Er^{3+}
Raman spectroscopy
Upconversion photoluminescence

ABSTRACT

This study analyzes the effects of doping $BaTiO_3$ with Er^{3+} within its perovskite ABO_3 structure, specifically investigating how substituting Er^{3+} at the Ba (A-site) and Ti (B-site) locations influences the material at different doping levels. Scanning electron microscopy (SEM)/energy-dispersive X-ray spectrometry (EDS) analysis shows that all of the samples have polygonal grains. In BTO doped with 0.01 wt% and 0.1 wt% Er^{3+} grain size was up to 45 μm. With the higher amount, the growth is slowing down and grains are 2–10 μm. Raman spectra show part of common $BaTiO_3$ modes only for the lowest content of Er^{3+}. At higher Er^{3+} content, the usual modes are completely covered by strong luminescence originating from Er^{3+} deexcitation from energy level $^2H_{11/2}$. The intensity of the photoluminescence (PL) bands shows the influence of not only the Er^{3+} concentration, but also the crystallinity of the sample, especially their surface. The FIR reflectivity shows a slight wavelength shift for higher sintering temperature, but all spectra show lower intensity comparing with pure $BaTiO_3$. FTIR transmission spectra show slight shifts of characteristic Ti–O bending mode at about 480 cm^{-1} confirming the incorporation of Er^{3+} in $BaTiO_3$ at 1320 °C and 1350 °C. Near IR excitation (1530 nm) provoked upconversion photoluminescent (UCPL) spectra of $BaTiO_3$:Er^{3+} with PL lines at higher energies. The upconversion mechanism for each line was determined and the fluorescence lifetime was estimated. It is observed that the obtained intensities of UCPL increase gradually at both sintering temperatures with increase of Er^{3+} content.

1. Introduction

Oxide materials, with chemical formula ABO_3, such as barium titanate ($BaTiO_3$) are known to belong to the perovskite family. The anion, mostly oxygen, is located in the center of the side of the cube [1]. The perovskite structure can be viewed as a cubic packing of A and O ions, with B ions filling the octahedral interstitial sites, but it can also be viewed as a three-dimensional structure composed of [BO_6] octahedra, which is shown in Fig. 1. Therefore, each of the eight barium ions belongs simultaneously to eight adjacent cells and each of the six oxygen ions is shared between two adjacent unit cells. In this sense, 8:8 = 1 barium ion and 6:2 = 3 oxygen ions belong to each titanium ion, from which the empirical formula $BaTiO_3$ follows.

Cubic $BaTiO_3$ has the properties of a paraelectric, upon cooling it changes to the tetragonal phase and becomes ferroelectric, and Ti^{4+} ions occupy positions outside the center of the octahedron [2]. The displacement of the oxygen and titanium ions leads to a slight distortion of the unit cell [3]. The axis along which the ions move is stretched while the remaining two are shortened, thus changing the cubic structure to a tetragonal one. This phase transition is accompanied by remarkable dielectric anomalies, the transition temperature is called Curie's point T_c [4]. Above 130 °C, these materials have a centrosymmetric cubic perovskite structure. However, as the temperature decreases, the structure goes through three characteristic phase transformations, each

* Corresponding author.
E-mail addresses: lzorica@yahoo.com, lzorica@ipb.ac.rs (Z.Ž. Lazarević).

https://doi.org/10.1016/j.optmat.2024.116581
Received 21 October 2024; Received in revised form 29 November 2024; Accepted 15 December 2024
Available online 17 December 2024

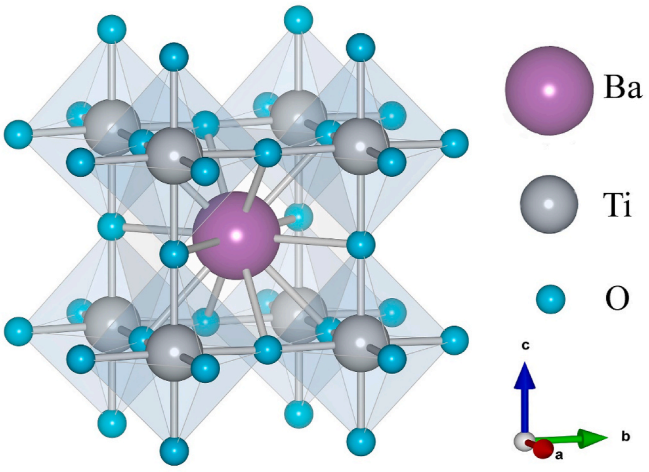

Fig. 1. The unit cell structure of pervoskite $BaTiO_3$.

of which involves a small distortion of the cubic unit cell. Barium titanate exists in several crystalline modifications, depending on the temperature [1]. The high-temperature phase (125–1460 °C) has a cubic (*Pm*3 *m*) structure, while below 130 °C the structure of $BaTiO_3$ is tetragonal (*P*4*mm*) [5].

These materials have been intensively studied since Wul and Goodman (1945) until today, precisely because of their excellent properties and the possibility of application in various branches of industry [6,7]. They are used for the production of components in electronic and electro-optical devices, such as multilayer ceramic capacitors, pyroelectric detectors, components for ferroelectric memory, sensors and thermistors with a positive temperature coefficient of resistance [6, 8]. The unique electrical and electromechanical properties of barium titanate ceramics can be modified by varying the sintering conditions and/or doping with different rare earth ions [9–14]. Therefore, additives are added to barium titanate powders for two reasons: 1. to influence the sintering process (densification and grain growth); 2. to develop the desired electrical and electro-optical properties. Numerous researchers have focused on trivalent lanthanides, particularly Er^{3+}, which has proven to be an excellent dopant with outstanding spectroscopic characteristics, especially in optical fibers [15–19]. Luminescent nanomaterials are promising candidates for establishing NTM, thanks to their high sensitivity, rapid signal acquisition, and minimally invasive nature of luminescence signal detection. Lanthanide ions, including Er^{3+}, Ho^{3+}, Nd^{3+}, and Yb^{3+} with near-infrared emissions, have been employed as emitters in optical nanothermometers for in vivo applications [20]. The trivalent erbium (Er^{3+}) ion is a commonly employed luminescent species to realize efficient up-conversion (anti-Stokes) emission [21,22].

It can be observed that the incorporation of ions at A or B sites in ABO_3 compounds significantly affects the Curie's temperature and other physical properties during the doping process [13,23]. Isovalent impurities, which have the same valence as the ions they replace, do not affect defect populations. However, anisovalent impurities, which have a different valence from the ions they substitute, necessitate the creation of charge compensation defects to preserve electrical neutrality. When the replacement cation has a lower valence than the original, electronic holes may form, whereas a higher valence replacement cation can lead to the release of electrons. For example, the Er^{3+} ion, with a valence and ionic radius intermediate between the Ba^{2+} ion and the Ti^{4+} ion, could theoretically substitute either A or B sites in $BaTiO_3$, depending on the Ba/Ti ratio [24,25]. When Er^{3+} is incorporated into $BaTiO_3$, the reaction can be represented as:

$$Er_2O_3\ (\text{en}\ BaTiO_3) \rightarrow 2Er^{\bullet}_{Ti} + 2O_o + (1/2)\ O_2\ (g) + 2e' \quad (1)$$

The influence of Er^{3+} as a dopant on BT is evident. The amount of added erbium during the doping process is very important. Among the various methods for preparing polycrystalline solids, the solid-state reaction method was used for the synthesis of doped BT. Solid-state reactions of mixed powders have numerous advantages compared to other methods, relating to cost-effectiveness, simplicity, and large-scale production [26].

2. Experimental procedure

The entire process of synthesis and the starting materials used to obtain $BaTiO_3$ ceramics doped with Er^{3+}, we have presented in detail in our earlier work [25,27, 28]. The samples of Er_2O_3 doped $BaTiO_3$ were prepared by conventional solid-state sintering procedure starting from high purity commercial $BaTiO_3$ powder (MURATA) with Ba and Ti ratio, [Ba]/[Ti] = 1.005, and reagent grade Er_2O_3 powder (Fluka chemika). The content of additive oxides, Er_2O_3, is ranged from 0.01 to 1.0 wt%.

The initial powders were mixed and ground together in an ethyl alcohol medium for 24 h. This milling process was carried out using a polypropylene container and zirconia balls, each with a diameter of 10 mm, as the grinding media. After milling, the slurries were placed in an oven at 200 °C and dried until they reached a stable weight. PVA was then mixed in as a binder. The resulting powders were compressed into disks with a diameter of 7 mm and a thickness of 3 mm using a uniaxial pressure of 120 MPa. These disks were sintered in an air atmosphere at temperatures of 1320 °C and 1350 °C for 4 h. During the sintering process, the temperature was raised at a rate of 5 °C per minute and reduced at a rate of 10 °C per minute.

The samples were treated with a solution of 10 % HCl and 5 % HF for microstructural analysis. The microstructures of both the as-sintered and chemically etched samples were examined using a scanning electron microscope (JEOL-JSM 5300) with an attached energy dispersive spectrometer (EDS-QX 2000S system). The grain size and porosity distribution in the samples were measured using the LEICA Q500MC Image Processing and Analysis System.

The NTEGRA Prima system, provided by NT-MDT, was used for the atomic force microscopy (AFM) analysis. Topographical images were captured in semi-contact mode using NSG01 probes from NT-MDT. The conditions under which the topographical images were obtained are: semi-contact mode (NSG01 probe from NT-MDT), curvature radius of 10 nm, force of 6 N, and frequency of 150 kHz. All measurements are performed under ambient conditions.

The BOMMEM DA-8 FIR spectrometer was used to record FT-IR spectra. A DTGS detector was employed in the experiment. All measurements are displayed in the band from 90 to 650 cm^{-1}.

The Jobin Yvon T64000 spectrometer was utilized to record all Raman spectra in a backscattering configuration, featuring a nitrogen-cooled CCD detector. A Ti laser with a wavelength of 514.5 nm and an output power of 20 mW served as the excitation source. All spectra were displayed in the band from 100 to 2200 cm^{-1}.

To successfully analyze the Er^{3+} doped $BaTiO_3$ ceramic obtained through sintering at different temperatures (1320 and 1350 °C) we used the FTIR spectroscopy method. The name of the device used was: ATR-FTIR Nicolet™ IS™ 10 Thermo Scientific, Waltham, MA, USA. The measurements are displayed in the band from 400 to 1100 cm^{-1} with a resolution of 0.5 cm^{-1}.

The upconversion photoluminescence (UCPL) experiments described in this study were carried out at ambient temperature using a Q-switched Er-doped glass laser operating at 1535 nm with nanosecond pulses (≤6 ns) and a pulse energy of 500 μJ. Time-resolved streak images of the upconversion emission spectra were acquired with a SpectraPro 2300i spectrograph and recorded using a Hamamatsu C4334 streak camera set to photon counting mode. The streak camera was operated with the HPD-TA software, and the analysis of fluorescence lifetimes was carried out using the TA-Fit program.

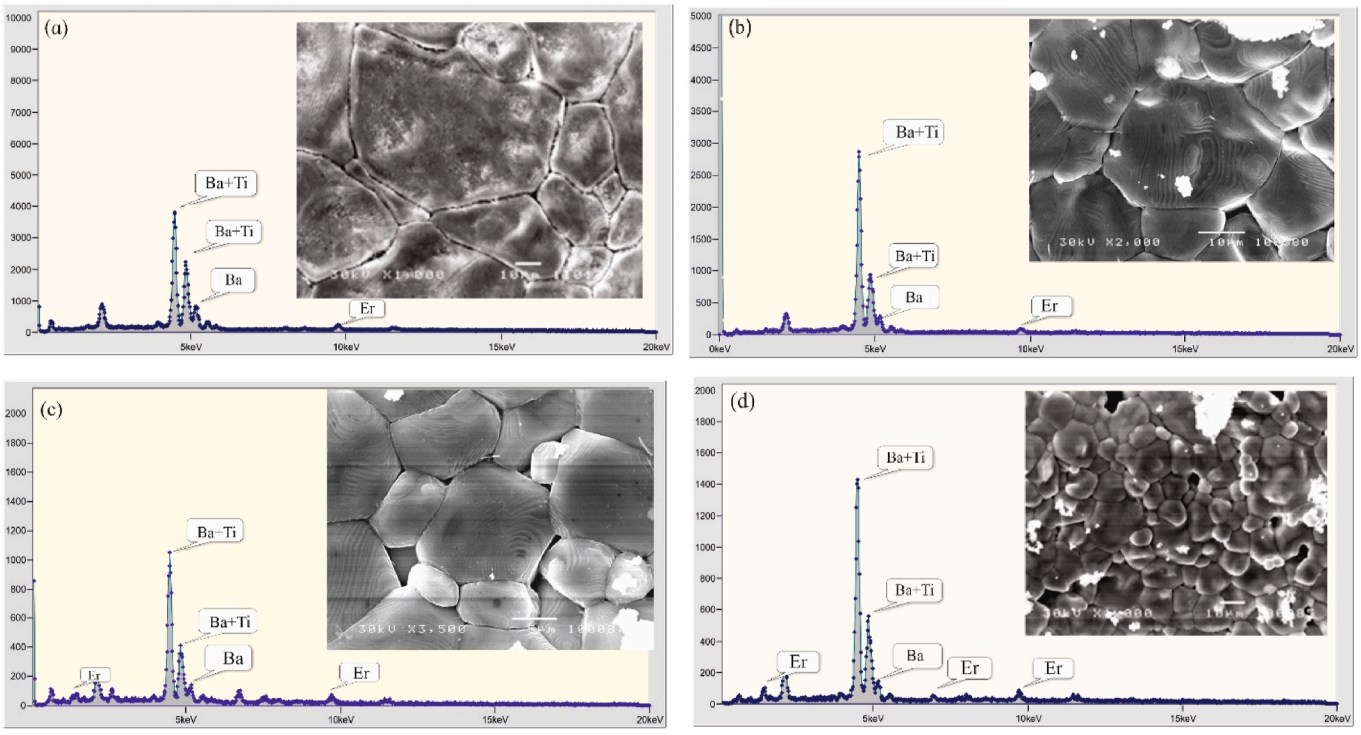

Fig. 2. EDS spectra with insets SEM images of $BaTiO_3$ doped with (a) 0.01, (b) 0.1, (c) 0.5 and (d) 1.0 wt% of Er^{3+} and sintered at 1320 °C.

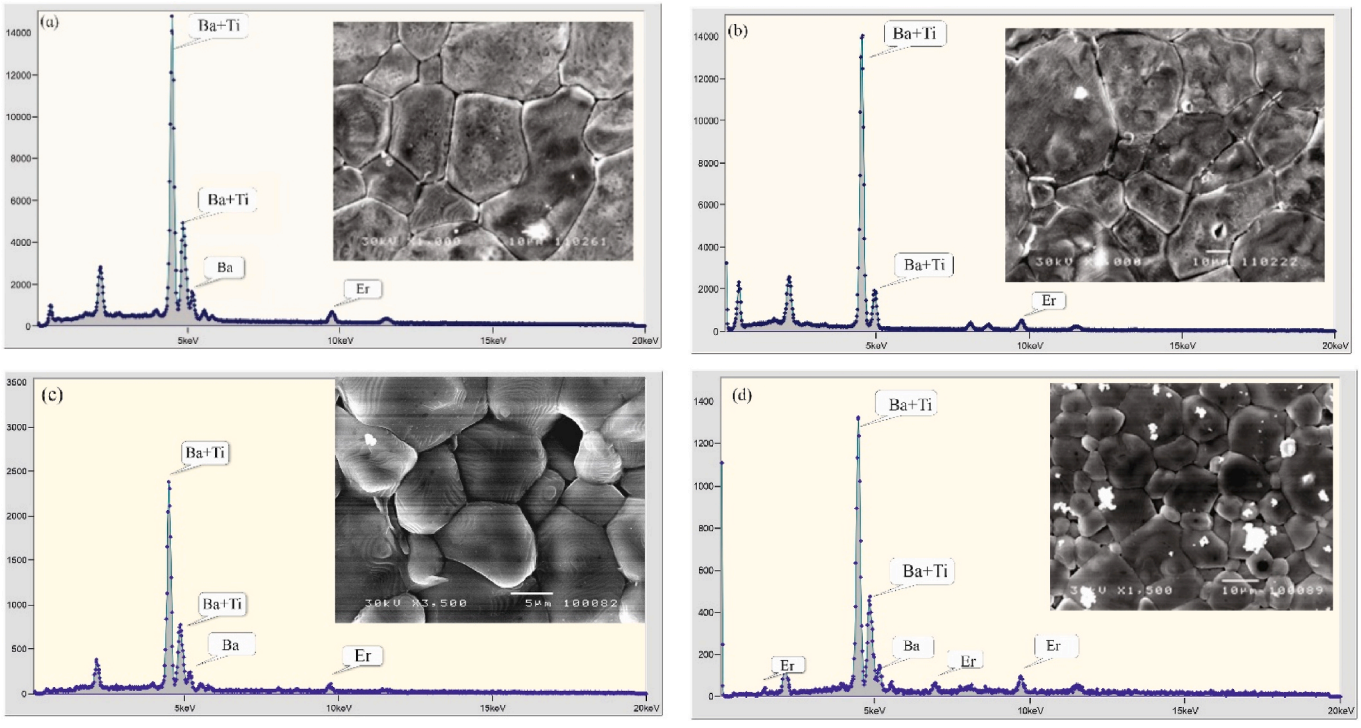

Fig. 3. EDS spectra with insets SEM images of $BaTiO_3$ doped with (a) 0.01, (b) 0.1, (c) 0.5 and (d) 1.0 wt% of Er^{3+} and sintered at 1350 °C.

3. Results and discussions

3.1. Structural and morphological characterization

X-ray diffraction analysis of $BaTiO_3$ samples doped with 0.01 wt% Er^{3+} reveals only the presence of the $BaTiO_3$ perovskite phase with a uniform distribution of erbium. When the doping concentration is increased to 0.5 wt% Er^{3+}, a secondary phase, $Er_2Ti_2O_7$, becomes noticeable. The shift in XRD peaks for the doped samples compared to undoped $BaTiO_3$ indicates that the lattice parameters have increased, suggesting that Er^{3+} ions are likely substituting for Ti rather than Ba in the $BaTiO_3$ structure.

The microstructural analysis of the Er^{3+}-doped $BaTiO_3$ ceramics shows irregular polygonal grains (*insets* Figs. 2 and 3). At lower doping

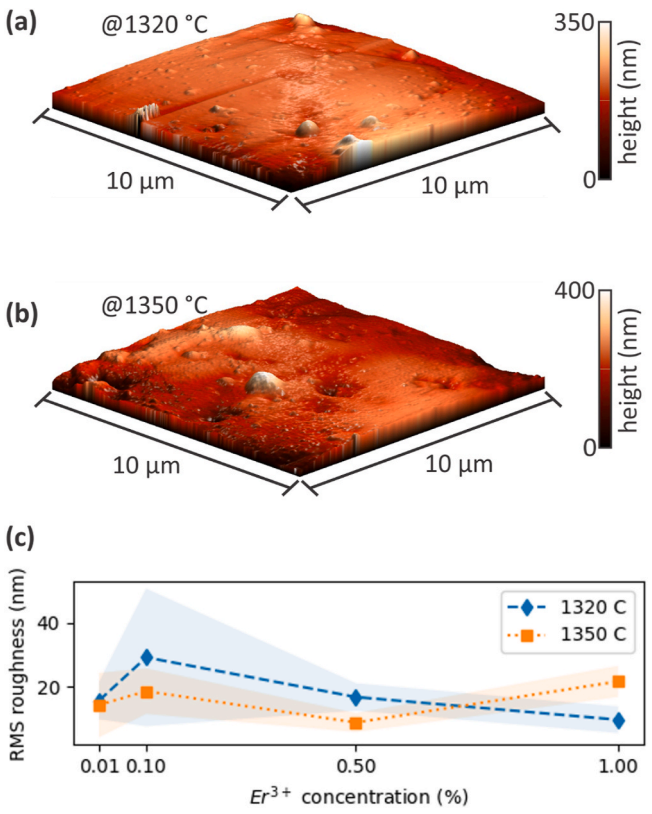

Fig. 4. AFM topography of a doped $BaTiO_3$ (a) (0.1 wt% Er^{3+}) grain for a sample sintered at 1320 °C. (b) (0.1 wt% Er^{3+}) grain for a sample sintered at 1350 °C. (c) Average RMS roughness as a function of Er^{3+} concentration for samples sintered at 1320 °C (diamond markers) and sintered at 1350 °C (square markers). The edges of (blue, orange) shaded areas represent the lowest and highest RMS roughness values at a given temperature for a particular Er^{3+} concentration. (For interpretation of the references to colour in this figure legend, the reader is referred to the Web version of this article.)

levels (0.01 wt% and 0.1 wt% Er^{3+}), the grains exhibit abnormal growth, ranging from 20 to 45 µm (Fig. 2(a) and (b); Fig. 3(a) and (b)). As the doping concentration rises, the average grain size decreases: for 0.5 wt% Er^{3+}, the size ranges from 10 to 15 µm, and for 1.0 wt% Er^{3+}, it further reduces to 5–10 µm (Fig. 2(c) and (d); Fig. 3(c) and (d)).

Figs. 2 and 3 show EDS diagrams with corresponding inset SEM images of $BaTiO_3$ samples doped with Er^{3+}. It can be noted that the BT sample with 0.01 wt% Er^{3+} shows that the erbium is evenly distributed throughout the material, with no visible erbium-rich areas. This uniform distribution is consistent with the limitations of EDS, which may not be able to detect lower concentrations effectively unless significant inhomogeneity occurs. At higher doping levels, erbium-rich regions begin to appear between the grains.

A large number of scientific papers describe microscopy methods for characterizing Er^{3+}-doped $BaTiO_3$, including the use of AFM [29]. It can be said that AFM is highly effective for examining the morphology and surface texture of various materials. This texture encompasses factors like roughness, waviness, orientation, and defects. With the appropriate software, AFM allows for the assessment of features such as surface roughness, porosity, average particle size, and distribution. These characteristics play a crucial role in determining the optical, mechanical, surface, magnetic, and electrical properties of materials.

The AFM is used to examine the surface of the grains. It can be said that AFM analysis involves examining topographic images of the grain surface and evaluating the RMS value to assess surface characteristics. The RMS roughness corresponds to the variation in height measurements taken by the AFM and is highly responsive to pronounced surface features such as valleys and peaks. Consequently, the RMS is used to estimate the flatness of the surface.

Few studies related to grain growth and surface analysis as a function of the doping concentration in $BaTiO_3$ have been carried out [30]. It is well known that the introduction of Er^{3+} ions due to the variation of size between Er^{3+} and Ti^{4+} ions result in a slight lattice distortion, however, the studies have shown that the variation in the concentration of the ions has an important contribution.

Examples of AFM topography images recorded within grains at two different synthesizing temperatures, 1320 °C and 1350 °C are shown in Fig. 4(a) and (b). Examining the topography images in Fig. 4(a) and (b) shows that there are no substantial variations in the grain structures across different Er^{3+} concentrations at either temperature. For each concentration, it is evident that the grain size decreases with increasing both, the dopant concentration and the thermal treatment. The surfaces are flat, with RMS values not exceeding 50 nm for every Er^{3+} concentration, as shown in Fig. 4(c). For each concentration, it is evident that the grain size decreases with increasing both, the dopant concentration and the thermal treatment. It can be noted that our AFM analysis is in agreement with Clabel et al. [30].

3.2. IR and Raman spectroscopic studies

The unit cell of $BaTiO_3$ comprises 5 atoms, which results in a total of 15 vibrational modes. At room temperature, the unit cell adopts a tetragonal, non-centrosymmetric structure with *P4mm* symmetry. Based on the group theory analysis, the vibrational modes of $BaTiO_3$ are:

$$\Gamma = 4A_1 + B_1 + 5E. \quad (2)$$

Among them, $1A_1$ and $1E$ are acoustic modes. All optical modes are Raman active and $3A_1$ and $4E$ are also IR active. The A_1 modes oscillate along the z-axis, while the E modes are confined to the *xy*-plane.

Consequently, the analysis of the polarized Raman spectra of $BaTiO_3$ (excluding the non-polar B_1 mode) serves as a complementary analysis to the far-infrared (FIR) reflectivity spectra.

As A_1 modes oscillate along the z-axis and the E modes are confined to the *xy*-plane, the overall reflectivity (R) can be expressed as the weighted sum of reflectivity contributions from these two orientations: reflectivity in the *xy*-plane (R_{xy}) and reflectivity along the *z*-axis (R_z). This relationship is given by:

$$R = \frac{2}{3}\cdot R_{xy} + \frac{1}{3}\cdot R_z. \quad (3)$$

Fig. 5 presents the IR reflectivity spectra for $BaTiO_3$ samples doped with 0.01 wt%, 0.1 wt%, 0.5 wt% and 1.0 wt% Er^{3+} and sintered at temperatures of 1320 °C and 1350 °C. The spectrum for pure $BaTiO_3$ [31] is also presented in Fig. 5 to emphasize the changes in the spectra resulting from the integration of Er into the crystal structure of $BaTiO_3$. All TO normal modes are stressed with blue upward arrows. Wei *at al.* [32] schematically illustrated the oscillations of all normal modes and assigned them according to the polarization of Raman modes determined by DiDomenico *at al.* on single domain crystals [33].

The $E(1)$TO mode, being the lowest energy soft mode, is especially important in the study of ferroelectric properties. This mode involves the oscillation of the O_6 octahedral framework relative to the central Ti atom along the *x* or *y* axis within the TiO_6 octahedron, producing a substantial dipole moment. Theoretical calculations for the soft $E(1)$TO mode give unrealistically high values, from 79 to 139 cm^{-1} [32,34,35], but according to experimental FIR reflectivity and Raman spectra, this value must be about 40 cm^{-1} [31,33,35]. $E(1)$LO is about 180 cm^{-1}.

Numerous researchers refer to the summary of optical phonon frequencies and their symmetries in tetragonal $BaTiO_3$ provided in Ref. [36] as a benchmark for $BaTiO_3$ polycrystals. Accordingly, we have also used data from this reference to denote the TO phonon modes.

The narrow $A_1(1)$ mode, with transverse (TO) and longitudinal (LO)

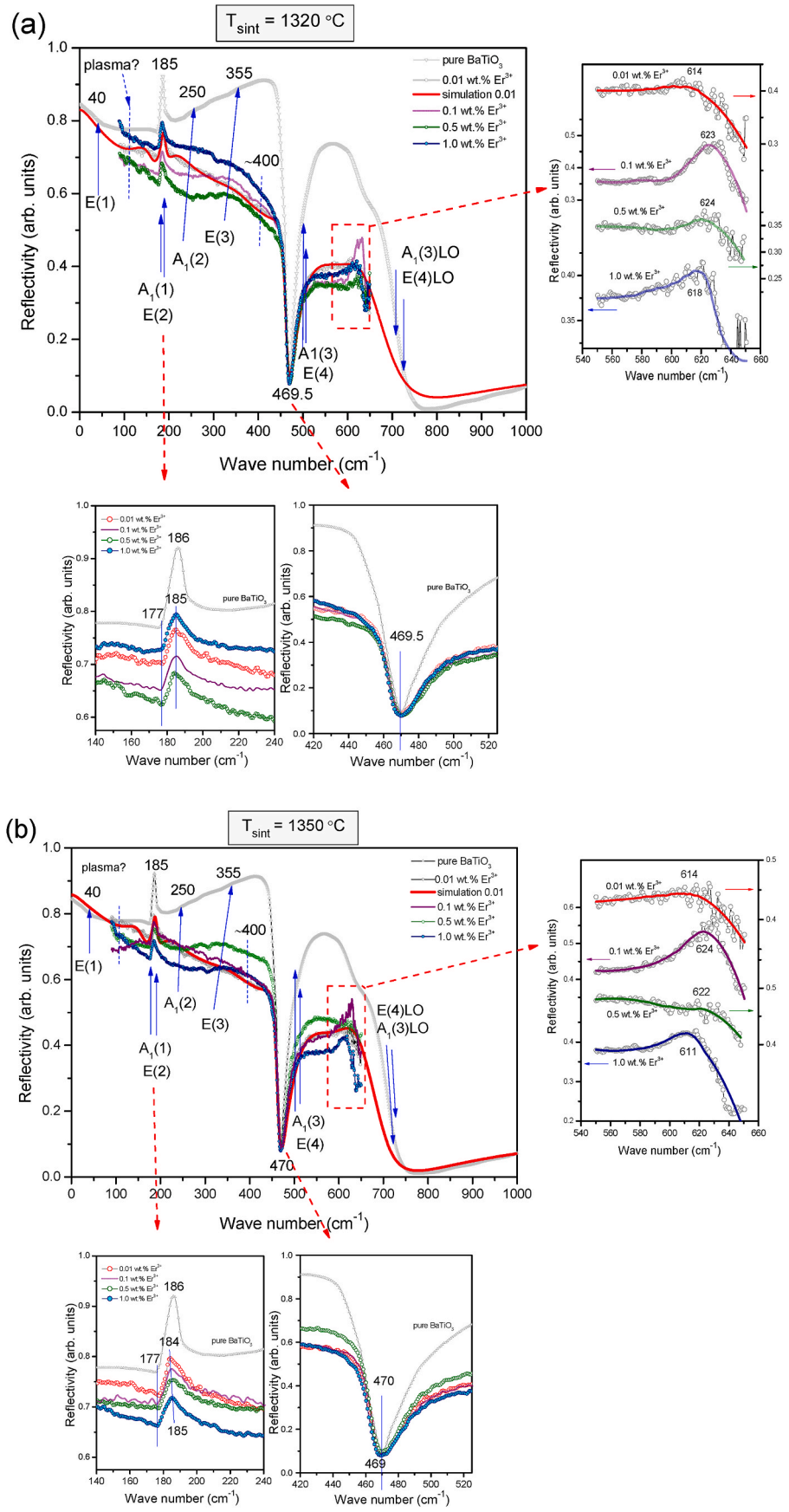

(caption on next page)

Fig. 5. IR reflectivity spectra of $BaTiO_3$ doped with 0.01; 0.1; 0.5 and 1.0 wt% of Er^{3+} and sintered at (a) 1320 °C and (b) 1350 °C. The spectrum of pure $BaTiO_3$ is added to highlight the differences caused by the incorporation of Er^{3+} into the $BaTiO_3$ crystal lattice. All TO normal modes are marked, and LO only for the last A_1, E pair with the highest wavenumbers. In the small figures on the right are details with "impurity" modes originating from structural imperfections. The solid lines are a guide to the eye obtained by smoothing the enormously disordered experimental spectra at the edge of the spectrometer range. Figures at the bottom give details of the two characteristic modes.

frequencies of approximately 170 and 185 cm^{-1}, respectively, can be interpreted as the vibration of the O_6 octahedral cage relative to the Ti atom along the *z* axis.

The $E(2)$ mode, with transverse (TO) and longitudinal (LO) frequencies around 180 and 305 cm^{-1}, describes the oscillation of the TiO_6 octahedron relative to Ba atoms within the *xy* plane. In contrast, the $A_1(2)$ mode, featuring TO and LO frequencies of approximately 270 and 475 cm^{-1}, is associated with the vibration of the TiO_6 octahedron relative to Ba atoms along the *z* axis. Additionally, the $E(3)$ mode, with TO and LO frequencies of about 305 and 463 cm^{-1}, has a longitudinal wave number that is quite similar to that of the $A_1(2)$ mode. The $E(4)$ and $A_1(3)$ modes have TO wave numbers at 486 and 520 cm^{-1} and LO at 715 and 720 cm^{-1}.

As can be seen, the modes are highly correlated, A_1 and E modes partially overlap, some values of different TO/LO modes are very close or even identical. Thus, it is appropriate to independently analyze the A_1 and E modes and compute the reflectivity using the previously mentioned Eq. (3).

Fig. 5 shows the complicated FIR spectra of doped polycrystalline $BaTiO_3$, with hinted plasma mode at the beginning. Semiconductor properties are expected in the doped samples and free charge carriers, i. e. plasma mode, surely exist in FIR reflectivity spectra. Incorporation of the heavy Er^{3+} ions, with an ionic radius of 0.89 Å, into the $BaTiO_3$ crystal lattice -where they replace either Ba^{2+} (with a radius of 1.61 Å), or Ti^{4+} (with a radius of 0.75 Å) – also leads to additional vibrational modes [37]. This is attributed to the resulting lattice disorder mostly caused by the size mismatch. Applying the fitting procedure to such complex spectra could give a good match of the fit and experiment, but the result would be difficult to explain. For each sintering temperature, we fitted one reflectivity spectrum (for $BaTiO_3$ with 0.01 wt% Er^{3+}) to simulate the assumed plasma mode at short wave numbers and, at the same time, the LO modes at high wavenumbers that are outside the measured range. The Decoupled Plasmon - Phonon model [38,39] was used only for simulating the spectra.

From the IR reflectivity spectra presented in Fig. 5, it is evident that the intensity of the spectra for Er-doped $BaTiO_3$ is lower compared to that of pure $BaTiO_3$. For the samples sintered at 1320 °C, no changes in the frequencies of the normal vibrational modes were detected, except for the impurity modes observed between 614 and 624 cm^{-1}, as shown in Fig. 5(a). The observed variation in spectrum intensity with different Er^{3+} concentrations is unusual. Notably, the sample doped with 1.0 wt% Er^{3+} exhibits the highest intensity. This anomaly could be attributed to the surface condition of the samples, which significantly affects the intensity of the FIR reflectivity spectra. In the IR reflectivity spectra for doped samples that were sintered at 1350 °C, as depicted in Fig. 5(b), the normal modes exhibit minor shifts that correlate with the concentration of Er^{3+} ions. A noticeable variation in the intensity of the doped spectra occurs as a result of changes in the size of the crystal grains.

In Ref. [40] an extensive and detailed study of $BaTiO_3$:Er^{3+} was given in which it was analysed how the incorporation of Er^{3+} affects the appearance of Raman spectra. The following was concluded:

- Raman spectra of $BaTiO_3$ with Er at titanium sites have an appearance typical of tetrahedral pure $BaTiO_3$.
- The unusual appearance and intensity of the Raman spectra can be attributed to the incorporation of Er^{3+} in place of barium.
- The creation of a defect complex between Er at the sites of barium and titanium leads to a decrease in the intensity of the spectrum.

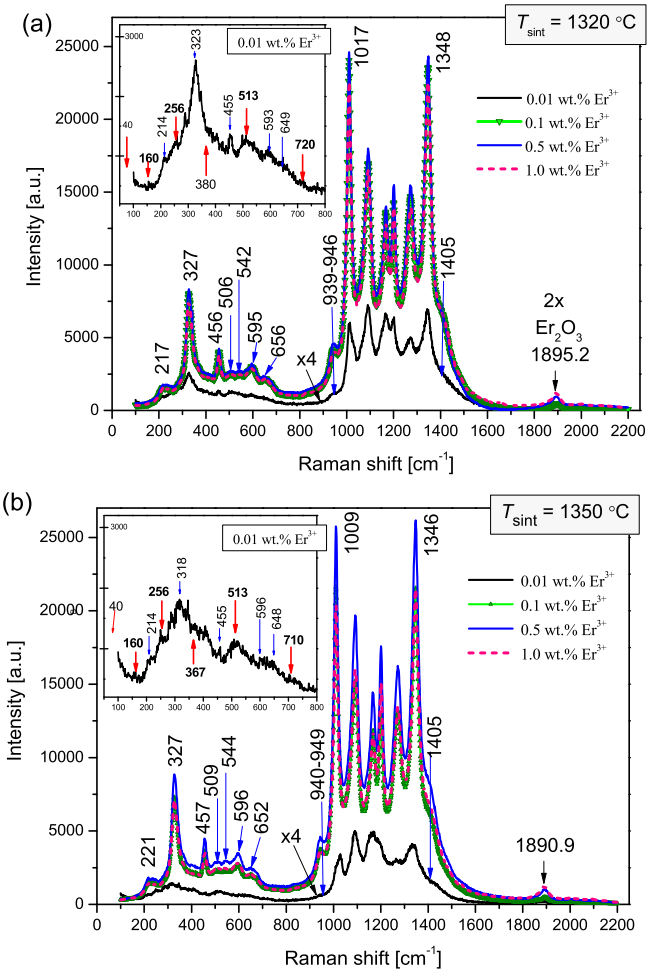

Fig. 6. Abnormal Raman spectra of $BaTiO_3$ doped with 0.01; 0.1; 0.5 and 1.0 wt% of Er^{3+} and sintered at (a) 1320 °C and (b) 1350 °C. Raman spectra were excited by λ = 514.5 nm Ar-ion laser line. In each insert is part of the $BaTiO_3$ spectrum with the lowest dopant level that has some features as common Raman spectrum. Visible normal modes are stressed by red arrows. (For interpretation of the references to colour in this figure legend, the reader is referred to the Web version of this article.)

- The unusual Raman signals were confirmed to be due to the fluorescence of Er^{3+} ions at the barium sites. The intensity of these fluorescence signals was so high that it overshadowed the conventional Raman spectra of $BaTiO_3$.

Raman spectra of all examined samples of $BaTiO_3$:Er^{3+} (wt.% Er^{3+} = 0.01, 0.1, 0.5, 1.0) sintered at 1320 °C and 1350 °C, activated by Ar-laser emission of λ = 514.5 nm, are shown in Fig. 6. As can be seen, the obtained spectra for both sintering temperatures have an abnormal Raman spectrum shape.

According to Da-Yong Lu *at al.* [40], it can be concluded that the largest part of Er^{3+} in our samples is incorporated in Ba-sites. The spectra of $BaTiO_3$ with the lowest concentration of Er^{3+} (0.01 wt%) are noticeably lower in intensity and with different spectral features compared to the spectra of samples with more Er^{3+}. *Inset* shows part of the spectrum of the sample with 0.01 wt% Er^{3+}. All normal Raman

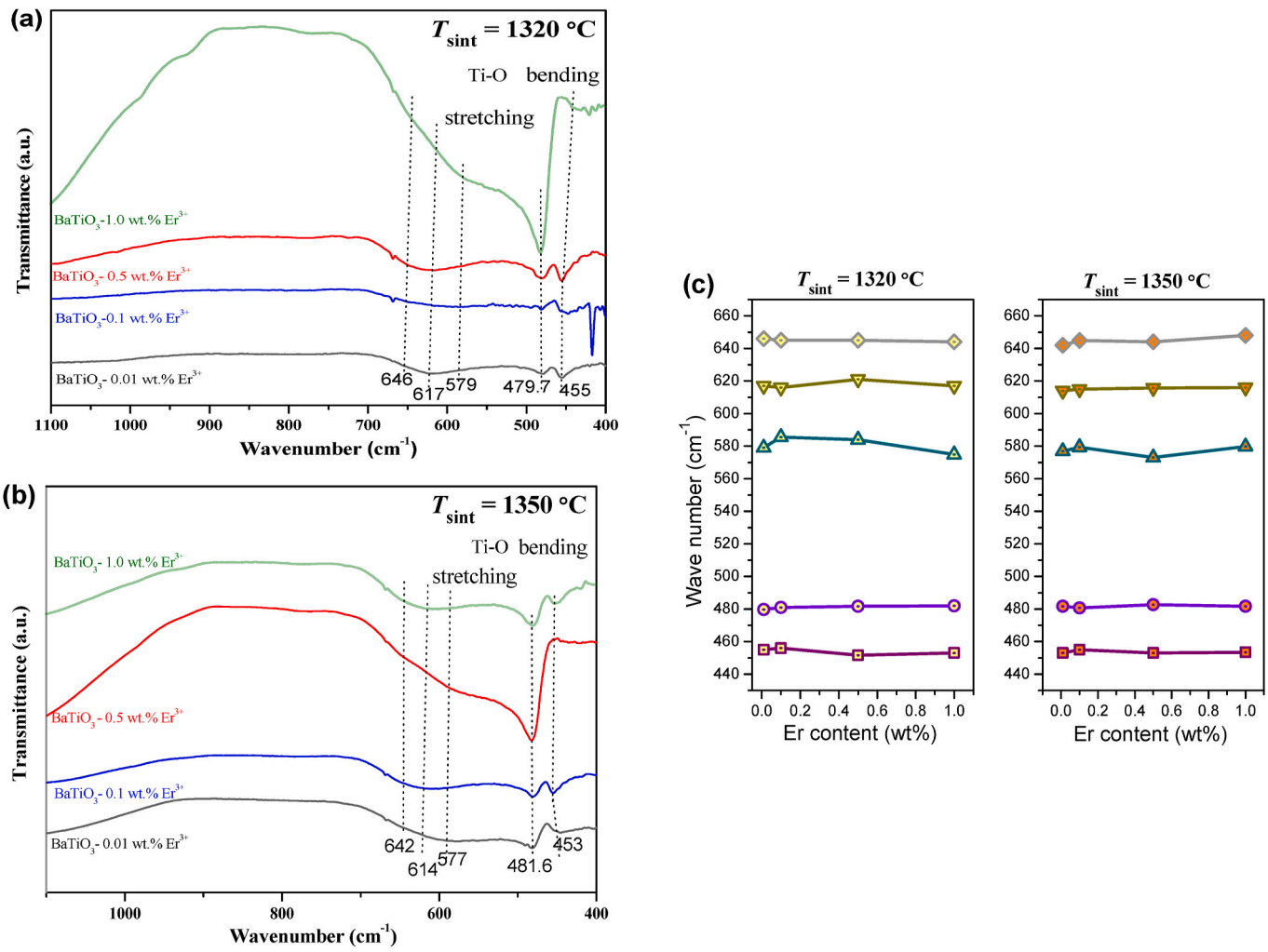

Fig. 7. FTIR spectra of $BaTiO_3$ doped with 0.01; 0.1; 0.5 and 1.0 wt% of Er^{3+} and sintered at (a) 1320 °C and (b) 1350 °C. (c) Shift of bending and stretching Ti–O modes with increasing dopant content at 1320 °C and 1350 °C.

modes of pure $BaTiO_3$ should be in the wavenumber range below 800 cm^{-1}, in the range of *inset*. Several normal Raman modes can also be observed in lightly doped $BaTiO_3$:Er^{3+}. At wave numbers below the measured range, it is supposed to be E(1)TO "soft" mode and at 160 cm^{-1} its LO-component is observed. At 256 cm^{-1} A_1(2)TO mode is present, and at 513 cm^{-1}, the E(4)TO and A_1(3)TO modes are observed. Hardly visible E(4)LO and A_1(3)LO modes are at 720 cm^{-1}. Mentioned modes, highlighted by red arrows, are partially obscured by a stronger fluorescence signal. Broad peaks are noted at 380 cm^{-1} (Fig. 6(a), *inset*) and at 367 cm^{-1} (Fig. 6(b), *inset*), likely due to structural imperfections from Er incorporation into the Ti-sites of $BaTiO_3$ [36]. Fluorescence peaks at 214, 323, 455, 593 and 649 cm^{-1} (blue arrows) show certain red shift comparing to peaks in the samples with higher concentration of Er^{3+}. These fluorescence peaks are a part of the transitions from the excited state of Er^{3+} ion to the eight Stark components of its $^4I_{15/2}$ ground state [13]. At wavenumbers from 800 cm^{-1} to 1700 cm^{-1}, in the stronger fluorescent transition, all eight peaks are clearly visible and remain at unchanged positions regardless of the Er^{3+} concentration (including 0.01 wt% Er^{3+}).

The intensity levels of the Raman spectra, or rather to say fluorescence spectra, of the $BaTiO_3$ samples with 0.1, 0.5, and 1.0 wt% Er^{3+}, that are sintered at 1320 °C, differ very little from each other, while in the case of higher sintering temperature, the intensity difference is striking, see Fig. 6. In both cases, Raman spectra with 0.5 wt% Er^{3+} have the highest intensity, followed by spectra with 0.1 wt% and 1.0 wt% Er^{3+}.

The low intensity of the spectra doped by 0.01 wt. Er^{3+}, show that Er^{3+} ions are incorporated in both Ti– and Ba–sites forming the self-compensated $Er_{Ba}^{\cdot}$ – $Er_{Ba}^{\prime}$ defect complexes [40]. With a certain dopant concentration (depending on the structure, number of vacancies …) the fluorescence would be quenched. A similar thing happens when $BaTiO_3$ is doped with other rare earth ions [41].

Spectra of $BaTiO_3$ with larger amounts of Er^{3+} in the range of normal Raman modes (below 800 cm^{-1}) are significantly stronger in intensity and have clearly defined sharp fluorescent peaks, which proves that Er^{3+} is predominantly incorporated in Ba-sites. Significantly enhanced fluorescence peaks are in the range of Raman shift 900-1600 cm^{-1} (at about 690 cm^{-1} higher wave numbers). The appearance of the obtained Raman spectra of BTO samples doped with Er^{3+} resembles the up-conversion photoluminescence recorded in the photoluminescence spectra of $BaTiO_3$ doped with rare earth ions [40–43].

However, when the doped samples are excited with an energy of 514.5 nm (2.41 eV), the Er^{3+} ions, from its $^4I_{15/2}$ ground state, are directly elevated to $^2H_{11/2}$ state [40]. The fluorescence green transitions in our spectra originate from de-excitation of Er^{3+} from the nearest lower energy levels: $^2H_{11/2} \rightarrow {}^4I_{15/2}$ (centred at about 526 nm – in the range of normal Raman spectra) and $^4S_{3/2} \rightarrow {}^4I_{15/2}$, centred at 547 nm – at about 690 cm^{-1} higher Raman shift. (In absolute wave numbers, 690 cm^{-1} is subtracted from the 514.5 nm excitation laser line, i.e. 19436.4 cm^{-1}, and 18746.4 cm^{-1} is obtained, i.e. a lower value in absolute wave

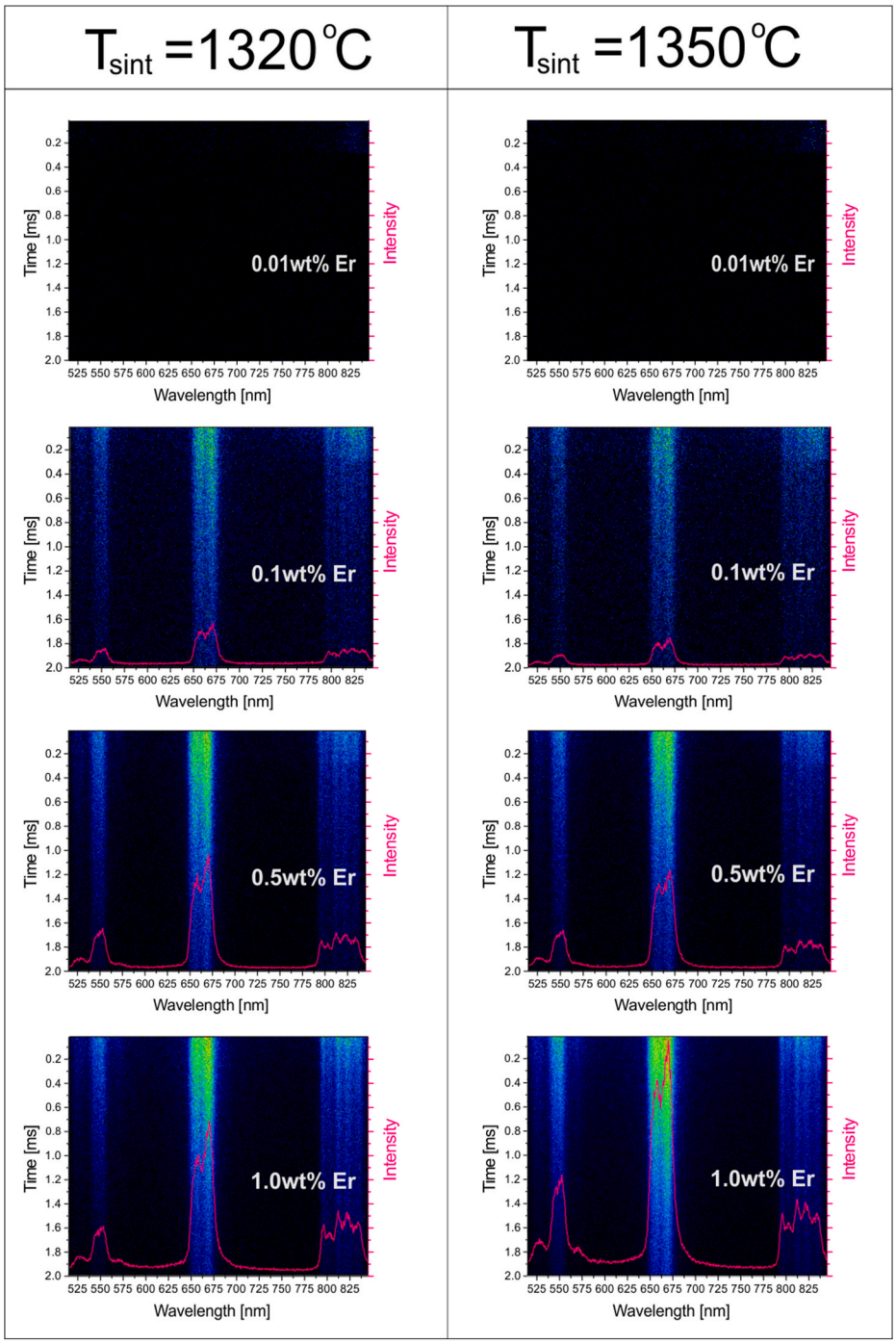

Fig. 8. Upconversion photoluminescence (UCPL) spectra of the $BaTiO_3$ doped with 0.01; 0.1; 0.5 and 1.0 wt% of Er^{3+} at two sintering temperatures (1320 °C and 1350 °C). Under the streak images are extracted figures of the relative PL peaks intensity.

numbers.) At higher Raman shifts, beyond the range of our measurement, are few red fluorescence transitions.

3.3. Fourier transform infrared spectroscopy

In tetragonal, non-centrosymmetric structure with P4mm symmetry all optical modes are IR and, at the same time, Raman active (except non-polar B1) mode that is only Raman active), Eq. (2). In Raman spectra are seen separated TO and LO modes. In polycrystalline $BaTiO_3$: Er^{3+}, due to already superimposed normal modes from two polarizations and a lot of weak modes caused by disturbed structure, an addition spectroscopic method is necessary that would allow a better insight into the details of the BTO spectrum changed by doping. Fourier transform infrared spectroscopy (FTIR) shows only TO modes, so it can simplify the analysis of vibrational modes in polycrystalline BTO.

Fig. 7 shows the FTIR spectra recorded on sintered samples of $BaTiO_3$ doped with Er^{3+}. Fig. 7(a) displays the spectra obtained from samples sintered at 1320 °C, whereas the spectra for samples sintered at 1350 °C are shown in Fig. 7(b). A shoulder can be observed in all spectra (in the range of 1000 to 900 cm^{-1}). It can also be confirmed that this originates from barium and titanium oxides [43]. Ti–O stretching modes are present around 600 cm^{-1} (three broad bands) and at 480 cm^{-1}. Bending Ti–O mode is around 455 cm^{-1}. These modes confirm that synthesized Er^{3+} doped $BaTiO_3$ samples have tetragonal structure for both sintering

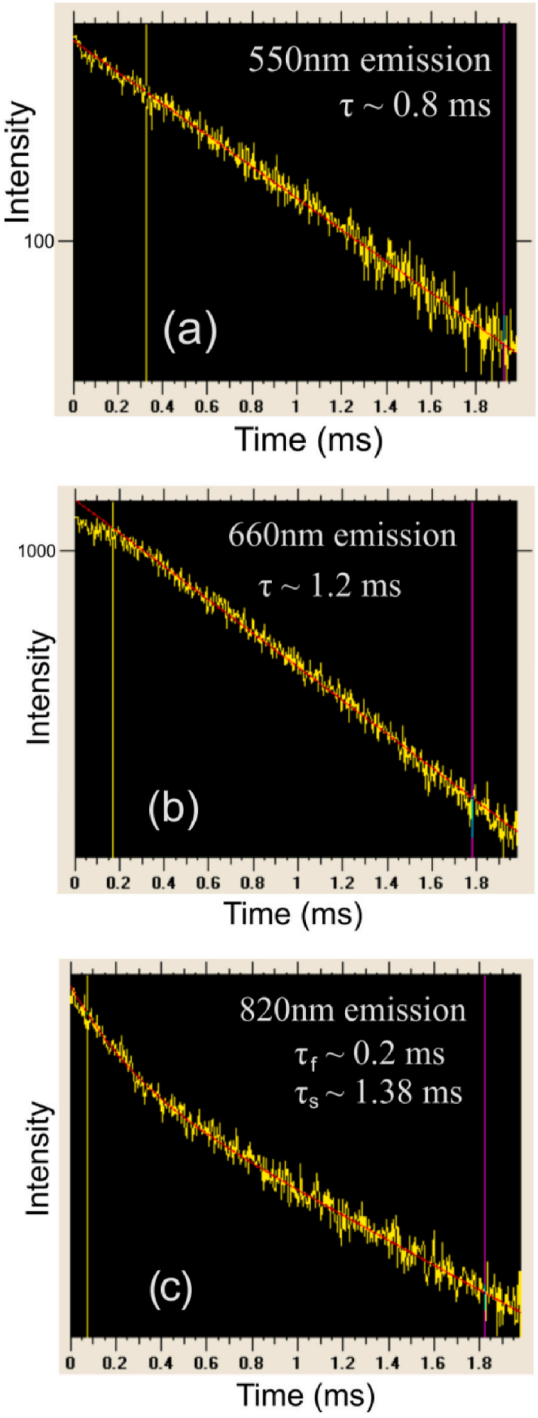

Fig. 9. Decay curves of the time-resolved UCPL emissions of (a) green, (b) red and (c) near infrared emission upon 1530 nm excitation of the 1.0 wt% Er^{3+}. The fitting curves, as well as the decay lifetimes are presented. (For interpretation of the references to colour in this figure legend, the reader is referred to the Web version of this article.)

temperatures [44–46]. However, peak positions are both the sintering temperature and the Er^{3+} concentration dependent, indicating differences in lattice distortions, presumably as a consequence of cation doping at different places [47].

At very low levels of Er^{3+} (0.01 and 0.1 wt%), the larger Er^{3+} ions replace the smaller Ti^{4+} ions in the crystal lattice. This substitution generally lengthens and weakens the bonds in the octahedral sites, which would typically result in a reduced oscillation frequency. Nonetheless, the introduction of Er^{3+} at these low levels also induces atypical crystal grain growth. This anomalous growth enhances the overall crystal structure, which in turn leads to an increase in the oscillation frequency.

With a continued increase in Er^{3+} concentration, the Ti sites become fully occupied, prompting Er^{3+} to substitute for Ba^{2+} ions. In this process, Er^{3+}, which has a much larger ionic radius, starts to replace Ba^{2+} at these larger sites. If we compare the doped $BaTiO_3$ with a content of 0.01 wt% and 0.1 wt% Er, we would notice that this results in a decrease in the lattice constant. Consequently, in samples sintered at 1320 °C, the oscillation frequency predominantly decreases, whereas samples sintered at 1350 °C exhibit a slight increase in frequency (see Fig. 7(c)). These observations indicate that the incorporation of Er^{3+} into $BaTiO_3$ can be adjusted by varying both the sintering temperature and the concentration of the dopant.

3.4. Photoluminescence

We have measured time-resolved upconversion photoluminescence spectra to demonstrate the effect of different Er^{3+} concentrations on $BaTiO_3$ at sintering temperatures of 1320 °C and 1350 °C. The obtained spectra are captured as streak images using the photon counting technique and are shown in Fig. 8. After NIR excitation (1530 nm), we have obtained the fluorescence spectra with temporal development on the y-axis which is the main advantage of streak images. As shown in Fig. 8, with increasing Er^{3+} concentration, the displayed intensities of UCPL gradually increase at both temperatures. Many studies have investigated and measured the upconversion processes in erbium, all aiming to improve the utilization of this dopant in different optical and in-vivo applications [48–50]. The primary mechanisms behind upconversion include two types of absorption (ground state and excited state), as well as potential energy transfer, which depends on the concentration. The red emission results from the interplay of the excited state, energy transfer, and the cross-relaxation process [51].

From our spectra (Fig. 8), it can be observed that some emissions are stronger when compared (the red is more intense than the green). At 1530 nm (mostly through ground state absorption (GSA)), Er^{3+} ions are excited and transition to the $^4I_{13/2}$ level. is mainly achieved through ground state absorption using near-infrared radiation at a wavelength of 1530 nm. Subsequently, the $^4F_{9/2}$ state is populated through two sequential processes involving two photons of 1530 nm and non-radiative relaxation. This is followed by a radiative transition to the ground state ($^4I_{15/2}$), leading to red emission at 660 nm. Excitations at 808 nm and 980 nm result in increased green emission [43,48,52], while excitation at 1530 nm produces stronger red emission [44]. Under 1550 nm excitation, stronger red emissions are most likely caused by cross relaxation process, which increases the population of $^4F_{9/2}$ levels [50, 51]. Certainly, the concentration of dopants and the energy transfer between them within the material have a significant effect on all the internal processes occurring in the material.

The upconversion photoluminescence decay curves of the 1.0 wt% of Er^{3+} at two sintering temperature 1350 °C at 550 nm, 660 nm and 820 nm are presented in Fig. 9. We found that the most accurate fitting results were obtained by applying a single exponential model to the decay profiles associated with the transitions at 550 nm ($^4S_{3/2}$ - $^4I_{15/2}$) and 660 nm ($^4F_{9/2}$ - $^4I_{15/2}$) of Er^{3+} ions, as illustrated in Fig. 9(a) and (b). The obtained fitted values of the fluorescence lifetimes are 0.8 ms for 550 nm, and 1.2 ms for 660 nm. The fluorescence decay at 820 nm ($^4I_{9/2}$ - $^4I_{15/2}$) reveals both slow and rapid components, as demonstrated in Fig. 9(c). The decay curve has been successfully represented using a biexponential model. The value obtained for the short-lived component of the lifetime is 0.2 ms, whereas the long-lived component is 1.38 ms. We can observe a trend that the lifetime is longer at higher emission wavelengths. Our estimation of lifetimes agrees well with the values in the work of Wang et al. [50].

4. Conclusion

By applying a standard synthesis procedure at sintering temperatures of 1320 and 1350 °C, we produced $BaTiO_3$ ceramics with varying concentrations of Er^{3+}.The microstructure and the optical properties were investigated. Methods such as XRD, SEM, Raman and FTIR spectroscopy were used for the characterization of the obtained samples. Also, the incorporation of Er^{3+} into barium titanate was demonstrated using EDS characterization methods. At Er^{3+} concentrations of 0.01 and 0.1 wt%, SEM shows large polygonal grains (10–25 μm). At 0.5 wt% Er^{3+}, grain growth is reduced, with sizes of 2–10 μm. SEM images suggest Er^{3+} solubility in $BaTiO_3$ is between 0.1 and 0.5 wt%. The infrared reflectivity and ATR-FTIR spectroscopy patterns indicate the characteristic bands relating to $BaTiO_3$. Modes shift slightly with increase of Er content in $BaTiO_3$, only 1-2 cm^{-1}, but not uniform due to simultaneous change in morphology of crystal grains with change in Er^{3+} concentration. The unusual RS can be used to detect the presence of Er^{3+} at the Ba sites in doped $BaTiO_3$. It has been shown that the effect of sintering temperature on the optical properties of doped $BaTiO_3$ is significant. The best observations were for the peaks ($^4S_{3/2}$ - $^4I_{15/2}$ and $^4F_{9/2}$ - $^4I_{15/2}$). Also, for $^4I_{9/2}$ - $^4I_{15/2}$ are two clearly visible a slow and a fast component with value lifetime 1.38 ms and, 0.2 ms, respectively. The results showed that temperature has a significant impact on the optical properties of Er^{3+}-doped $BaTiO_3$.

CRediT authorship contribution statement

Zorica Ž. Lazarević: Writing – original draft, Visualization, Supervision, Methodology, Investigation, Formal analysis, Conceptualization. **Aleksandra Milutinović:** Writing – review & editing, Visualization, Formal analysis. **Milica Ćurčić:** Methodology. **Maja S. Rabasović:** Writing – review & editing, Methodology, Formal analysis. **Ivana Stajčić:** Writing – review & editing, Methodology, Formal analysis. **Boško Ćosić:** Methodology. **Uroš Ralević:** Writing – review & editing, Methodology, Formal analysis. **Novica Paunović:** Methodology. **Branka Hadžić:** Methodology. **Bojana Simović:** Methodology. **Dalibor Sekulić:** Methodology. **Vesna Paunović:** Formal analysis, Investigation, Methodology, Writing – review & editing.

Declaration of competing interest

The authors declare that they have no known competing financial interests or personal relationships that could have appeared to influence the work reported in this paper.

Acknowledgments

The authors wish to thank the Institute of Physics Belgrade, Vinča Institute of Nuclear Sciences (Contract No. 451-03-66/2024-03/200017), the University of Belgrade, and the Faculty of Electronic Engineering at the University of Niš (Grant No. 451-03-65/2024-03/200102) for their financial support, which was facilitated by the Ministry of Science, Technological Development, and Innovation of the Republic of Serbia. This study was also funded by the Science Fund of the Republic of Serbia under Grant No. 7504386 for the project titled "Nano Object in Own Matrix – Self Composite – NOOM-SeC."

Data availability

Data will be made available on request.

References

[1] S. Pradhan, G.S. Roy, Researcher 5 (3) (2013) 60–62, https://doi.org/10.7537/marsrsj050313.10.
[2] M. Acosta, N. Novak, V. Rojas, S. Patel, R. Vaish, J. Koruza, G.A. Rossetti Jr., J. Rödel, Appl. Phys. Rev. 4 (2017) 041305, https://doi.org/10.1063/1.4990046.
[3] G.C. Manika, K.S. Andrikopoulos, G.C. Psarras, Molecules 25 (11) (2020) 2686, https://doi.org/10.3390/molecules25112686.
[4] Z. Chlup, D. Drdlík, H. Hadraba, O. Ševeček, F. Šiška, J. Erhart, K. Maca, J. Eur. Ceram. Soc. 43 (4) (2023) 1509–1522, https://doi.org/10.1016/j.jeurceramsoc.2022.11.030.
[5] E. Chávez, S. Fuentes, Ramón A. Zarate, L. Padilla-Campos, J. Mol. Struct. 984 (1–3) (2010) 131–136, https://doi.org/10.1016/j.molstruc.2010.09.017.
[6] M. Pérez-Labraa, F.R. Barrientos-Hernández, J.P. Hernández-Lara, J.A. Romero-Serrano, M. Reyes-Pérez, V.E. Reyes-Cruz, J.C. Juárez-Tapia, G. Urbano-Reyes, Rev. Metal. (Madr.) 54 (4) (2018) e129, https://doi.org/10.3989/revmetalm.129.
[7] M.M. Vijatovic, B.D. Stojanovic, J.D. Bobic, T. Ramoska, P. Bowen, Ceram. Int. 36 (6) (2010) 1817–1824, https://doi.org/10.1016/j.ceramint.2010.03.010.
[8] A.J. Moulson, J.M. Herbert, Electroceramics: Materials, Properties and Applications, second ed., John Wiley & Sons Ltd., New York, 2003 https://doi.org/10.1002/0470867965.
[9] L.V. Maneeshya, P.V. Thomas, K. Joy, Opt. Mater. 46 (2015) 304–309, https://doi.org/10.1016/j.optmat.2015.04.036.
[10] D. Hamdi, D. Talantikite-Touati, A. Manseri, A.T. Khodja, A. Souici, Opt. Mater. 152 (2024) 115387, https://doi.org/10.1016/j.optmat.2024.115387.
[11] A. Nfissi, Y. Ababou, M. Belhajji, S. Sayouri, L. Hajji, M.N. Bennani, Opt. Mater. 122 (2021) 111708, https://doi.org/10.1016/j.optmat.2021.111708.
[12] A. Madani, M. Alghamdi, B. Alamri, S. Althobaiti, Opt. Mater. 137 (2023) 113480, https://doi.org/10.1016/j.optmat.2023.113480.
[13] Y. Zhang, J. Hao, C.L. Mak, X. Wei, Opt Express 19 (3) (2011) 1824–1829, https://doi.org/10.1364/OE.19.001824.
[14] Y. Zhang, J. Hao, J. Appl. Phys. 113 (8) (2013) 184112, https://doi.org/10.1063/1.4805050.
[15] Y. Tsur, T.D. Dunbar, C.A. Randall, J. Electroceram. 7 (1) (2001) 25–34, https://doi.org/10.1023/A:1012218826733.
[16] P. Yongping, Y. Wenhu, Ch Shoutian, J. Rare Earths 25 (Supp. 1) (2007) 154–157, https://doi.org/10.1016/S1002-0721(07)60546-8.
[17] A.M. Markom, M.C. Paul, A. Dhar, S. Das, M. Pal, S.K. Bhadra, S. Dimyati, M. Yasin, S.W. Harun, Optik 132 (2017) 75–79, https://doi.org/10.1016/j.ijleo.2016.12.041.
[18] K.C. Kao, Dielectric Phenomena in Solids, first ed., Elsevier Academic Press, USA, 2004, pp. 221–224.
[19] C.B. Carter, M.G. Norton, Ceramics Materials: Science and Engineering, first ed., Springer, USA, 2007 https://doi.org/10.1007/978-0-387-46271-4.
[20] Y. Wu, Fang Li, Y. Wu, H. Wang, L. Gu, J. Zhang, Y. Qi, L. Meng, N. Kong, Y. Chai, Q. Hu, Z. Xing, W. Ren, F. Li, X. Zhu, Nat. Commun. 15 (2024) 2341, https://doi.org/10.1038/s41467-024-46727-5.
[21] E.I. Madirov, S.V. Kuznetsov, V.A. Konyushkin, D. Busko, Bryce S. Richards, A. Turshatov, Adv. Opt. Mater. 12 (2024) 2303094, https://doi.org/10.1002/adom.202303094.
[22] B.S. Richards, D. Hudry, D. Busko, A. Turshatov, I.A. Howard, Chem. Rev. 121 (15) (2021) 9165–9195, https://doi.org/10.1021/acs.chemrev.1c00034.
[23] H.M. Chan, M.R. Harmer, D.M.L. Smyth, J. Am. Ceram. Soc. 69 (6) (1986) 507–510, https://doi.org/10.1111/j.1151-2916.1986.tb07453.x.
[24] K. Takada, H. Ichimura, D.M. Smyth, Jpn. J. Appl. Phys. 26 (1987) 42–45.
[25] V.V. Mitic, Z.S. Nikolic, V.B. Pavlovic, V. Paunovic, M. Miljovic, B. Jordovic, L. Zivkovic, J. Am. Ceram. Soc. 93 (1) (2010) 132–137, https://doi.org/10.1111/j.1551-2916.2009.03309.x.
[26] J.P. Hernández Lara, M. Pérez Labra, F.R. Barrientos Hernández, J.A. Romero Serrano, E.O. Ávila Dávila, P. Thangarasu, A. Hernández Ramirez, Mater. Res. 20 (2) (2017) 538–542, https://doi.org/10.3989/revmetalm.129.
[27] V. Paunović, V.V. Mitić, M. Đorđević, M. Marjanović, Lj Kocić, Sci. Sinter. 49 (2017) 129–137, https://doi.org/10.2298/SOS1702129P.
[28] V. Paunović, V.V. Mitić, Lj Kocić, Ceram. Int. 42 (10) (2016) 11692–11699, https://doi.org/10.1016/j.ceramint.2016.04.087.
[29] J.L.H. Clabel, I.T. Awan, V.A.G. Rivera, I.C. Nogueira, M.A. Pereira-da-Silvaa, M. Siu Lia, S.O. Ferreira, E. Marega Jr., Appl. Surf. Sci. 493 (2019) 982–993, https://doi.org/10.1016/j.apsusc.2019.07.003.
[30] J.L.H. Clabel, S.N. Nazrin, G.C. Lozano, M. Pereira da Silva, M. Siu Li, E. Marega Jr., Vacuum 194 (2021) 110562, https://doi.org/10.1016/j.vacuum.2021.110562.
[31] T. Ostapchuk, J. Petzelt, M. Savinov, V. Buscaglia, L. Mitoseriu, Phase Transitions 79 (6–7) (2006) 361–373, https://doi.org/10.1080/01411590600892047.
[32] Wei An, Liu Tian-Hui, Wang Chun-Hai, Diao Chuan-Ling, Luo Neng-Neng, Liu Yong, Qi Ze-Ming, Tao Shao, Wang Yu-Yin, Huan Jiao, Tian Guang-Shan, Jing Xi-Ping, Acta Phys. Chim. Sin. 31 (6) (2015) 1059–1068, https://doi.org/10.3866/PKU.WHXB201504144.
[33] M. DiDomenico Jr., S.H. Wemple, S.P.S. Porto, Phys. Rev. 174 (1968) 522–530, https://doi.org/10.1103/PhysRev.174.522.
[34] R.A. Evarestov, A.V. Bandura, J. Comput. Chem. 33 (2012) 1123–1130, https://doi.org/10.1002/jcc.22942.
[35] Huai-Yong Zhang, Zhao-Yi Zeng, Ying-Qin Zhao, Qing Lu, Yan Cheng, Z. Naturforsch. 71 (8) (2016) 759–768, https://doi.org/10.1515/zna-2016-0149, a.
[36] U.D. Venkateswaran, V.M. Naik, R. Naik, Phys. Rev. B 58 (1998) 14256, https://doi.org/10.1103/PhysRevB.58.14256.
[37] R.D. Shannon, Acta Crystallogr. A 32 (1976) 751–767, https://doi.org/10.1107/S0567739476001551.
[38] F. Gervais, B. Piriou, Phys. Rev. B 10 (1974) 1642–1654, https://doi.org/10.1103/PhysRevB.10.1642.
[39] F. Gervais, Mater. Sci. Eng. R 39 (2–3) (2002) 29–92, https://doi.org/10.1016/S0927-796X(02)00073-6.

[40] Lu Da-Yong, Wei Cheng, Xiu-Yun Sun, Liu Qiao-Li, Li De-Xu, Li Zhong-Yu, J. Raman Spectrosc. 45 (2014) 963–970, https://doi.org/10.1002/jrs.4575.
[41] Lu Da-Yong, Dong-Xue Guan, Sci. Rep. 7 (2017) 6125, https://doi.org/10.1038/s41598-017-06521-4.
[42] M. Vega S. Fuentes, I.R. Martín, J. Llanos, Mater. Res. Bull. 86 (2017) 95–100, https://doi.org/10.1016/j.materresbull.2016.10.001.
[43] A. Meneses-Franco, M. Campos-Vallette, S. Octavio Vásquez, E.A. Soto-Bustamante, Materials 11 (2018) 1950, https://doi.org/10.3390/ma11101950.
[44] H. Taher Elhmali, I. Stajcic, A. Stajcic, I. Pesic, M. Jovanovic, M. Petrovic, V. Radojevic, Polymers 16 (2024) 278, https://doi.org/10.3390/polym16020278.
[45] T. Xian, H. Yang, L. Di, M. Jinyuan, H. Zhang, D. Jianfeng, Nanoscale Res. Lett. 9 (2014) 327, https://doi.org/10.1186/1556-276X-9-327.
[46] M. Tihtih, J.E.F.M. Ibrahim, M.A. Basyooni, R. En-nadir, I. Hussainova, I. Kocserha, ASC Omega 8 (2023) 8448–8460, https://doi.org/10.1021/acsomega.2c07497.
[47] L. Ramajo, M.S. Catro, M.M. Reboredo, Compos. Appl. Sci. Manuf. 38 (2007) 1852–1859, https://doi.org/10.1016/j.compositesa.2007.04.003.
[48] R. Balda, N. Hakmeh, M. Barredo-Zuriarrain, O. Merdrignac-Conanec, S. García-Revolla, M.A. Arriandiaga, J. Fernández, Materials 9 (2016) 353, https://doi.org/10.3390/ma9050353.
[49] Y. Liu, Z. Zhou, S. Zhang, E. Zhao, J. Ren, L. Liu, J. Zhang, Nanomaterials 11 (2021) 2767, https://doi.org/10.3390/nano11102767.
[50] X. Wang, T. Li, W. Liang, C. Zhu, L. Guo, J. Am. Ceram. Soc. 104 (2021) 5826, https://doi.org/10.1111/jace.17974.
[51] A. Madhu, N. Srinatha, Infrared Phys. Technol. 107 (2020) 103300, https://doi.org/10.1016/j.infrared.2020.103300.
[52] P. Ghosh, S. Sadhu, T. Sen, A. Patra, Bull. Mater. Sci. 31 (2008) 461–465, https://doi.org/10.1007/s12034-008-0072-7.